

## **Contents of this file**

In this document, we provide material with supporting information to the manuscript. We include one additional text (Section S1) and five figures (Figure S1-S5), and three tables (Table S1-S3). Table S1 lists the focal depths and output information obtained with the surface waveform model of all 35 earthquakes. Table S2 shows the list of stations used in analysis, together their geographical coordinates. Table S3 presents the 1D velocity model based on CRUST1.0 package (Laske et al 2013) used in waveform modeling. Table S4 shows the parameters of the geodynamic modeling described in Text S1. Figure S1/2 shows the lithospheric age/low-density layer of the St. Paul transform system mapped by Maia et al (2016), parallelly. Figure S3 shows all earthquakes with  $M_w > 4.7$  cataloged since 1990 by the Global Centroid Moment Tensor catalog (Ekström et al. 2012). Figure S4 shows a map with the locations of all seismic stations listed on Table S2. Figure S5 shows the results of geodynamic thermal models described on Text S1.

## S1

### A geodynamic hydrothermal cooling model (HTCM)

HTCM obtains a steady-state temperature field from geodynamic thermal flow simulations of a 3D ridge-transform system using the geodynamic finite element code ASPECT (Bangerth et al., 2022). This model is built upon the methodology of Liu et al (2023) and involves a nonlinear viscoplastic mantle rheology. We implement the process of hydrothermal cooling over the top 6 km and up to 600 °C by adopting the methodology proposed by Morgan and Chen (1993). This process can efficiently cool the new oceanic crust by promoting more efficient heat loss from the crust (e.g., Morton and Sleep, 1985; Theissen-Krah et al., 2011). Hydrothermal cooling in the shallow brittle lithosphere is parameterized in terms of an effective thermal conductivity enhanced by a non-dimensional Nusselt number, which quantifies the relative efficiency of convective hydrothermal cooling in comparison to conductive heat loss.

In the geodynamic thermal model, the geometry of the transform system is extracted from the bathymetric observations of STPS including the lengths of transform segments A-D. Mantle flow is driven passively by imposing horizontal transform slipping rate of 27.8 mm/yr on the top boundary. All lateral boundaries and the bottom boundary are open so that materials can freely flow in and out of the model domain to maintain mass balance. The models are incompressible and therefore do not resolve thermal contraction and also do not account for viscous dissipation. The model setup is shown in Figure S4 and model parameters are listed in Table S3.

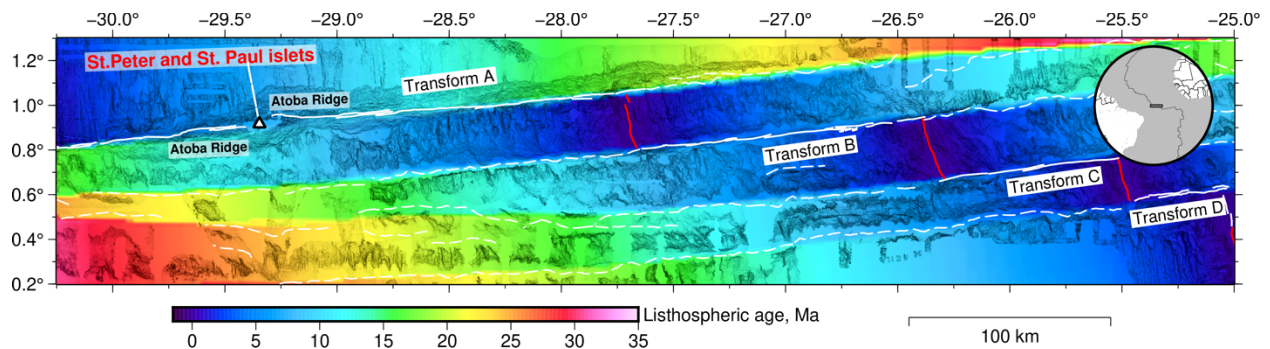


Figure S01 – Lithospheric age mapping of the St. Paul transform system (Maia et al 2016). Solid white lines represent the tectonic transform fault segments, with the dotted white lines indicating the fracture zones. Red lines refer to the intra-transform ridges. White triangle indicates the location of the St. Peter and St. Paul islets.

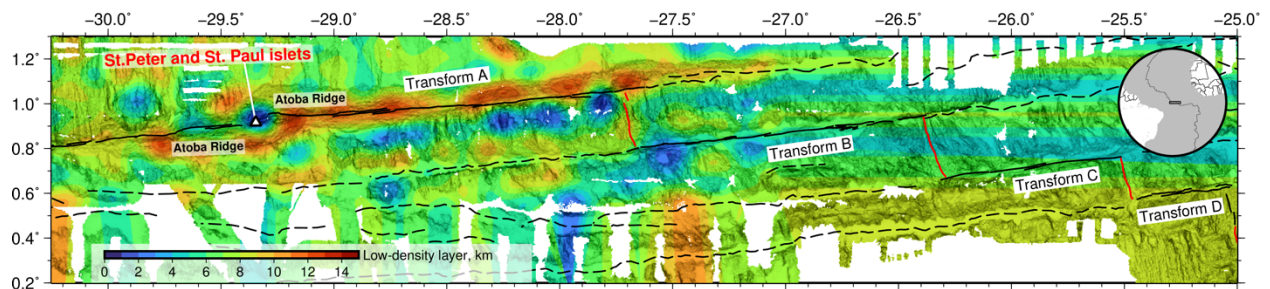


Figure S02 – Low-Density Layer mapping of the St. Paul transform system (Maia et al 2016). Solid white lines represent the tectonic transform fault segments, with the dotted white lines indicating the fracture zones. Red lines refer to the intra-transform ridges. White triangle indicates the location of the St. Peter and St. Paul islets.

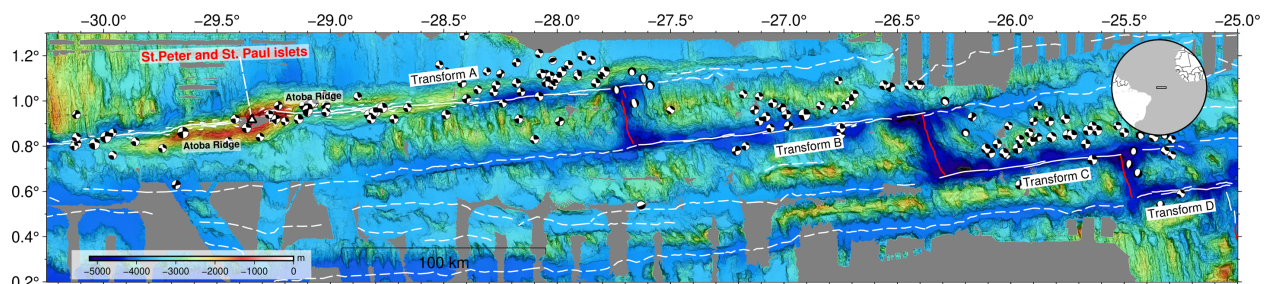


Figure S03 – Historical seismicity at St. Paul Transform System. Solid white lines represent the tectonic transform fault segments, with the dotted white lines indicating the fracture zones. Red lines refer to the intra-transform ridges. White triangle indicates the location of the St. Peter and St. Paul islets. Black beach balls refers to the historical earthquakes of the Global Centroid Moment Tensor catalog (Ekström et al. 2012) since 1990 with moment magnitude >4.7.

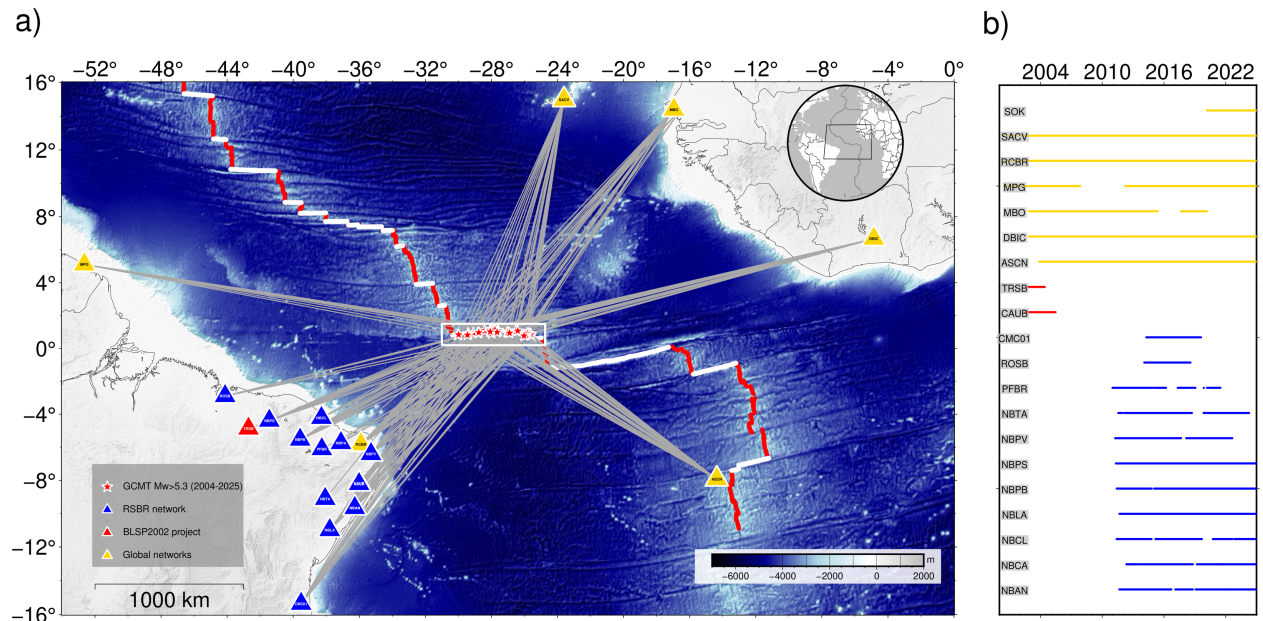
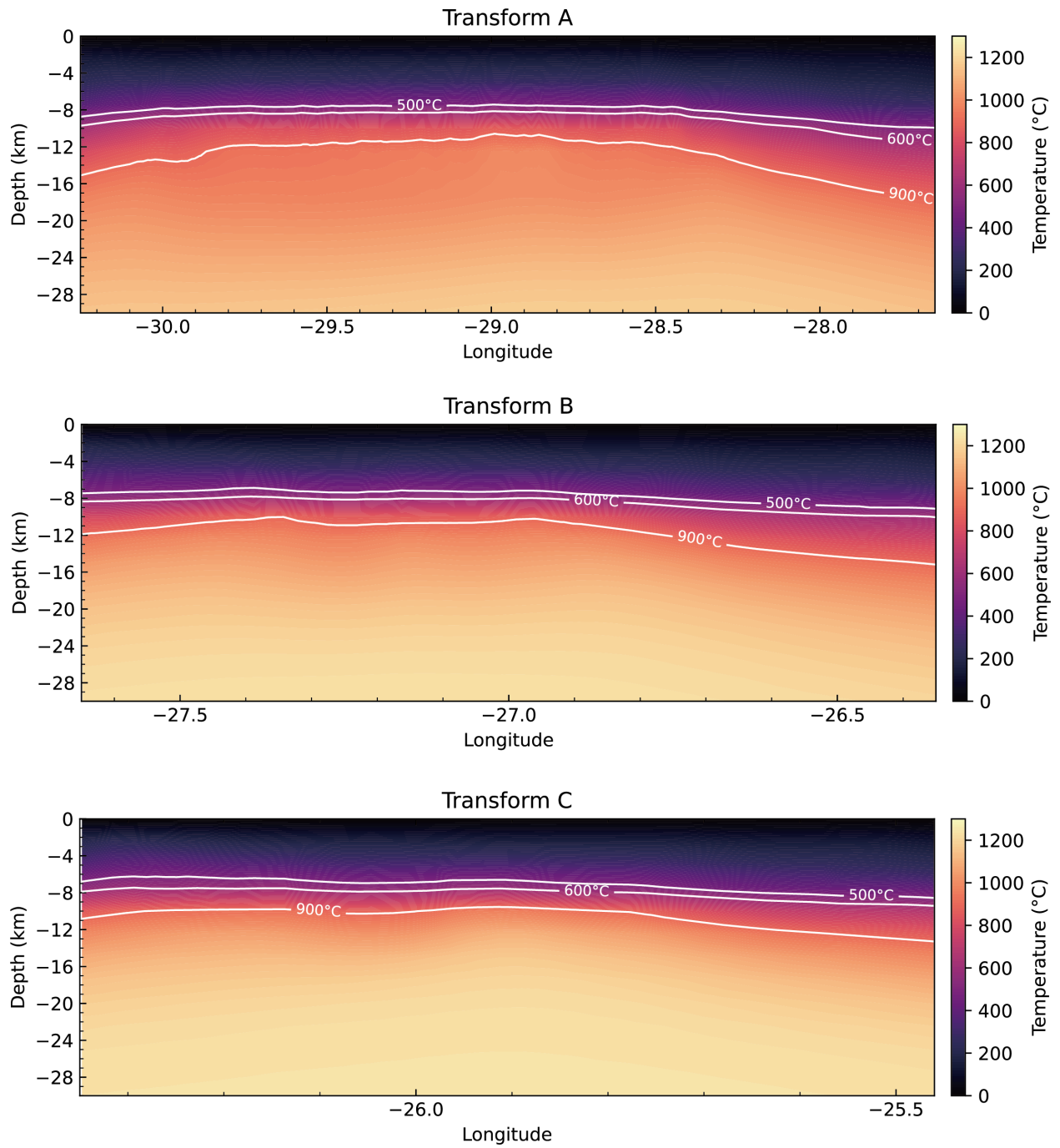


Figure S04 – A) Regional bathymetric map of the equatorial Atlantic with the locations of the 21 stations used in surface waveform modeling. Oceanic transform faults are presented by white lines, while the mid-ocean ridges are shown in red lines (Sautter et al. 2024). Red stars indicate the earthquakes of the Global Center Moment Tensor (GCMT) catalog with  $M_w > 5.3$ , used in the surface waveform model. The modeling was done using land and island stations of the Brazilian Seismographic network (RSBR, blue triangles, Bianchi et al. 2018), global stations of the Incorporated Research Institutions for Seismology network (IRIS/IDA, Scripps Institution of Oceanography, 1986), and GEOSCOPE networks (Romanowicz et al 1984) presented by the yellow triangles, and temporary land stations installed by the BLSP2002 project (Feng et al. 2004, red triangles). B) histogram showing the data availability of each station is shown on the right-hand side of the map. Gray lines represent the source-station ray paths of the GCMT earthquakes used in focal depth analysis.





*Figure S05 – Results of geodynamic thermal models with a nonlinear viscoplastic mantle rheology referent to Transform A, B, and C. Hydrothermal circulation is parameterized to activate in regions where the temperature falls below 600 °C and the depth is less than 6 km.*

## References

- Bangerth, W., Dannberg, J., Fraters, M., Gassmoeller, R., Glerum, A., Heister, T., et al. (2022). ASPECT: Advanced Solver for Problems in Earth's ConvecTion, User Manual. *Figshare*. <https://doi.org/10.6084/m9.figshare.4865333.v9>
- Bianchi, M. B., Assumpção, M., Rocha, M. P., Carvalho, J. M., Azevedo, P. A., Fontes, S. L., ... & Costa, I. S. (2018). The Brazilian seismographic network (RSBR): improving seismic monitoring in Brazil. *Seismological Research Letters*, 89(2A), 452-457. <https://doi.org/10.1785/0220170227>
- Ekström, G., Nettles, M., & Dziewoński, A. M. (2012). The global CMT project 2004–2010: Centroid-moment tensors for 13,017 earthquakes. *Physics of the Earth and Planetary Interiors*, 200, 1-9. <https://doi.org/10.1016/j.pepi.2012.04.002>
- Feng, M., Assumpcao, M., & Van der Lee, S. (2004). Group-velocity tomography and lithospheric S-velocity structure of the South American continent. *Physics of the Earth and Planetary Interiors*, 147(4), 315-331. <https://doi.org/10.1016/j.pepi.2004.07.008>
- Liu, S., Guo, Z., Rüpke, L. H., Morgan, J. P., Grevemeyer, I., Ren, Y., & Li, C. (2023). Sensitivity of gravity anomalies to mantle rheology at mid-ocean ridge–transform fault systems. *Earth and Planetary Science Letters*, 622, 118420. <https://doi.org/10.1016/j.epsl.2023.118420>
- Maia, M., Sichel, S., Briais, A., Brunelli, D., Ligi, M., Ferreira, N., ... & Oliveira, P. (2016). Extreme mantle uplift and exhumation along a transpressive transform fault. *Nature Geoscience*, 9(8), 619-623. <https://doi.org/10.1038/ngeo2759>
- Morgan, J. P., and Chen, Y. J. (1993). The genesis of oceanic crust: Magma injection, hydrothermal circulation, and crustal flow. *Journal of Geophysical Research: Solid Earth*, 98(B4), 6283-6297. <https://doi.org/https://doi.org/10.1029/92JB02650>
- Morton, J. L., & Sleep, N. H. (1985). A Mid-Ocean Ridge Thermal Model: Constraints on the volume of axial hydrothermal heat flux. *Journal of Geophysical Research: Solid Earth*, 90(B13), 11345–11353. <https://doi.org/10.1029/JB090iB13p11345>
- Sautter, B., Escartin, J., Petersen, S., Gaina, C., Granot, R., & Pubellier, M. (2024). *MAPRIDGES: global database of Mid-Oceanic ridges segments and transform faults*. *SEANOE*. <https://doi.org/10.17882/99981>
- Theissen-Krah, S., Iyer, K., Rüpke, L. H., & Morgan, J. P. (2011). Coupled mechanical and hydrothermal modeling of crustal accretion at intermediate to fast spreading ridges. *Earth and Planetary Science Letters*, 311(3), 275–286. <https://doi.org/10.1016/j.epsl.2011.09.018>